

# Universal Light-Driven Micro/Nanoscale Rotors

**Hongru Ding**

The University of Texas at Austin <https://orcid.org/0000-0003-1579-6825>

**Pavana Kollipara**

The University of Texas at Austin

**Abhay Kotnala**

The University of Texas at Austin

**Zhihan Chen**

The University of Texas at Austin

**Yuebing Zheng** (✉ [zheng@austin.utexas.edu](mailto:zheng@austin.utexas.edu))

The University of Texas at Austin <https://orcid.org/0000-0002-9168-9477>

---

## Article

**Keywords:** micro/nanoscale particles, universal light-driven rotation platform, optics

**Posted Date:** February 1st, 2021

**DOI:** <https://doi.org/10.21203/rs.3.rs-139439/v1>

**License:**  This work is licensed under a Creative Commons Attribution 4.0 International License.

[Read Full License](#)

---

# Universal Light-Driven Micro/Nanoscale Rotors

**Authors:** Hongru Ding<sup>1</sup>, Pavana Siddhartha Kollipara<sup>1</sup>, Abhay Kotnala<sup>1,2</sup>, Zhihan Chen<sup>2</sup>, and Yuebing Zheng<sup>1,2,\*</sup>

## Affiliations:

<sup>1</sup>Walker Department of Mechanical Engineering, The University of Texas at Austin, Austin, TX 78712, USA.

<sup>2</sup>Materials Science & Engineering Program and Texas Materials Institute, The University of Texas at Austin, Austin, TX 78712, USA.

\*Correspondence to: [zheng@austin.utexas.edu](mailto:zheng@austin.utexas.edu).

## Abstract

The capability of rotating micro/nanoscale particles and structures is important for micro/nanorobotics, three-dimensional particle imaging, and lab-on-a-chip systems. Light-driven rotors are especially attractive due to the fuel-free and remote operation. However, relying on a torque that arises from the momentum exchange with photons, current light-driven rotors require laser beams with designed intensity profile and polarization, or rotors with sophisticated shapes or material birefringence. These requirements hinder the light-driven rotation of many highly symmetric or isotropic particles, including biological cells, with simple optics. Herein, we report a universal approach to the out-of-plane rotation of various objects, including spherically symmetric and isotropic particles, using single arbitrary low-power laser beams. Moreover, the driving laser beam is positioned away from the rotors to reduce optical damage from the direct light illumination. The working mechanism of the rotors based on opto-thermo-electrical coupling is elucidated by systematic experiments combined with multiscale simulations. With its general applicability and simple optics, our universal light-driven rotation platform will become an essential component in various scientific research and engineering applications.

## Introduction

Micro/nanorotors or controlled rotation of micro/nanoscale objects play crucial roles in sensing, imaging, biomedicine, and manufacturing. They have proved effective in the detection of vacuum friction<sup>1</sup>, few-nanometer fabrication<sup>2</sup>, precise nanosurgery<sup>3</sup>, and microfluidic flow control<sup>4</sup>. Light-driven micro/nanorotors are promising due to their non-contact fuel-free operation<sup>5,6</sup>. The optical torque that drives a rotor originates from asymmetric absorption and scattering of light by the rotor. The rotation requires precise control of polarization<sup>1,7-9</sup> and intensity profile of the laser beams<sup>10-12</sup> or sophisticated design of geometry<sup>13,14</sup> and composition<sup>15-17</sup> of the rotor. The former often relies on complex optics to create designer laser beams that lead to the strong asymmetric light-rotor interactions and thus the large enough optical torques for the rotation<sup>13,18</sup>. In particular, to rotate homogenous and symmetric particles<sup>19</sup> and live cells<sup>20</sup>, multiple-beam optical tweezers were proposed. Moreover, optical torques are reduced significantly when the rotor size decreases<sup>21</sup>. The reduced torques make it challenging to precisely control nanorotors, which experience

strong Brownian motion in fluids. It has remained challenging for simple and low-power optics to achieve light-driven rotation of a wide range of objects, including optically symmetric synthetic particles and biological cells.

It becomes more challenging to achieve light-driven out-of-plane rotation (i.e., rotation of an object around an axis parallel to the substrate)<sup>22-24</sup>. Enabling three-dimensional (3D) interrogation, out-of-plane rotation of objects such as biological particles would provide an effective solution to single-cell engineering<sup>25</sup>, organism identification<sup>26</sup>, and microsurgery<sup>27,28</sup>. Recently, light-driven out-of-plane rotation has only been realized using dual-beam optical tweezers with a complex intensity profile<sup>10</sup>, or combining light with a microfluidic field<sup>29</sup> or an external electric field<sup>30</sup>. In a theoretical paper, Lou et al proposed the use of anisotropic optical trapping for out-of-plane rotation based on single-beam optical tweezers, which would require complex optics and high-power laser beams<sup>31</sup>. So far, out-of-plane rotors using single low-power laser beams have not been achieved.

Herein, we present a concept of opto-thermoelectric rotation (OTER), which harnesses optothermally generated electrokinetic force, depletion force and electric force to drive out-of-plane rotation of arbitrary micro/nanoparticles based on simple and low-power optics. We have even achieved the rotation of spherically symmetric and homogenous micro/nanoparticles using a single Gaussian laser beam of linear polarization and ultra-low power. Moreover, our driving laser beam is positioned away from the rotors to reduce the damage caused by the direct light illumination. Combining experiments with multiscale simulations, we reveal that the electrokinetic interaction between micro/nanoparticles and an optically heated substrate with thermo-responsive surface charge governs the particle rotation behaviors. To show the general applicability of our OTER strategy, we have demonstrated rotation of objects of diverse sizes (from subwavelength scale to micrometer scale), materials (biological, polymeric, dielectric, and composite colloids) and shapes (aspect ratios ranging from 1 to 8) using a low-power Gaussian laser beam. The rotor behaviors such as rotation speed, rotation axis, and particle-laser distance can be tailored on-demand through the control of colloidal chemistry and incident light.

## **Working mechanism of universal light-driven rotors**

The experimental setup and working mechanism of OTER is illustrated in Fig. 1. By directing a laser beam to a light-absorbing substrate (a porous Au film as an example, see Methods and Supplementary Fig. 1 for details), a tailorable temperature field can be established in the aqueous solution containing the rotor, which is represented as a spherical particle in Fig. 1a. To optothermally generate the forces and torque required for the stable rotation of the rotor, we added polyethylene glycol (PEG) molecules and phosphate buffered saline (PBS) into water and functionalized the substrate with carboxylic-acid-terminated alkanethiol self-assembled monolayers (COOH-SAMs) (Fig. 1b(i)). The particle and substrate possess negative surface charges (see Supplementary Fig. 2) due to ionized carboxyl, phosphoric acid or hydroxyl groups (also see Supplementary Note 1 for zeta potential measurements).

Without optical heating, the particles, ions, molecules are randomly dispersed in the solution with uniform temperature distribution. Upon a laser beam of wavelength corresponding to the absorption peak of the substrate used, a maximum temperature rise of  $\sim 9$  K (simulated temperature distribution, also see Supplementary Note 2 for measured temperature distribution) was obtained as illustrated in Fig. 1b. The light-generated temperature gradient results in the spatial separation of  $\text{Na}^+$  and  $\text{Cl}^-$  ions (which are the major ingredients of PBS) and thus creates a thermoelectric

(TE) field (Fig. 1b(ii)), which drives the thermo-electrophoresis of the charged rotor. We should note that the thermal polarization of water molecules results in an opposite TE field, but the direction of accumulative TE field is dominated by ionic charge separation<sup>32</sup>. Accordingly, a repulsive TE force ( $F_{TE}$ ) acts on the negatively charged particle. Meanwhile, the temperature gradient leads to a concentration gradient of PEG molecules due to thermal diffusion of the molecules. As a result, an osmotic-pressure-induced attractive depletion force ( $F_D$ ), which is directed towards the hot region, is acted on the rotor (Fig. 1b(i))<sup>33,34</sup>.

To generate torque on the particle for its rotation, we further exploited the surface charge gradients on the substrate and the rotor under the light irradiation to provide optothermally tunable electrokinetic force (named as thermo-electrokinetic force). Specifically, the acid dissociation constant of carboxylic acid,  $K$ , is sensitive to the temperature as well. According to van't Hoff equation,  $d\ln(K)/dT = \Delta H^\ominus/RT^2$ , where  $T$  is environmental temperature and  $\Delta H^\ominus$  is standard enthalpy change<sup>35</sup>;  $K$  decreases when temperature is increased because the dissociation of carboxylic acid is exothermic, i.e.,  $\Delta H^\ominus$  is negative<sup>36</sup>. In the light-generated non-uniform temperature field, a carboxylic acid molecule in the low-temperature region is prone to dissociate into a conjugate base,  $R-COO^-$ , and a hydrogen ion,  $H^+$  (Fig. 1b(iii)), leading to a gradient of the surface charge on the substrate.

With a non-uniform negative surface charge (with the smaller magnitude of charge in the hot region), the substrate exerts a thermo-electrokinetic force with upward  $z$  component and  $x$  component towards the hot region on the rotor. The surface charge on the particles with ionized acid groups is also non-uniform. Due to the asymmetric distribution of surface charges on both the substrate and particle, the line of action of the thermo-electrokinetic force does not pass through the centroid of the particle (see Supplementary Fig. 3 for the visualization of the discrete thermo-electrokinetic force). The thermo-electrokinetic force can be decomposed into a force ( $F_E$ ) passing through the centroid of the particle and a torque ( $M_E$ ) that drives the rotation as shown in Fig. 1b(iv). The balance among the depletion, TE, and thermo-electrokinetic forces passing through the centroid can be attained at a suitable rotor-light distance, where the thermo-electrokinetic torque drives a steady rotation of the rotor.

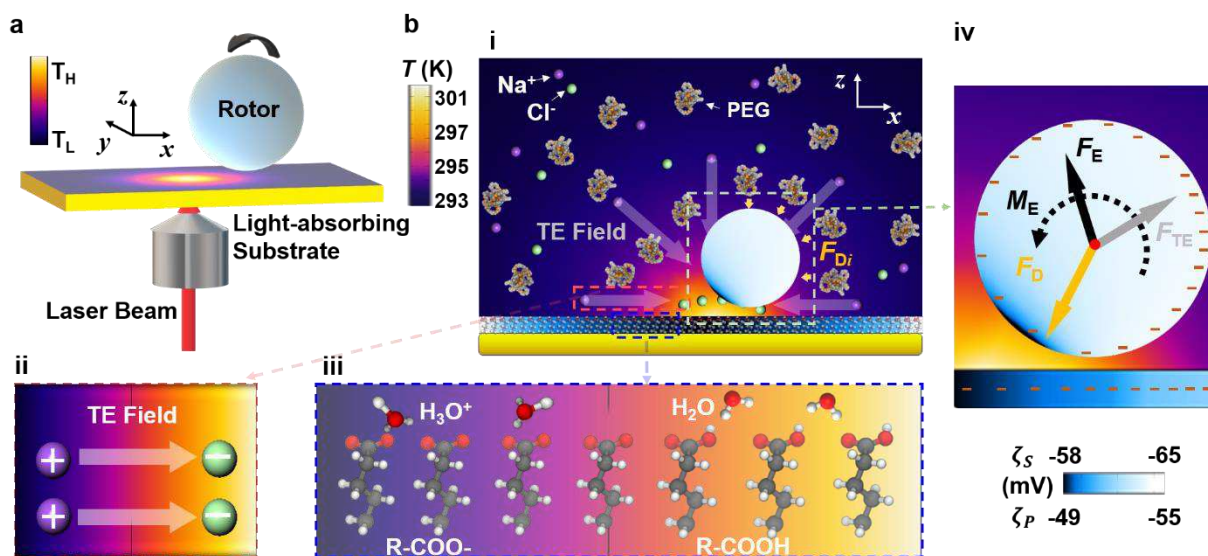


**Fig. 1** Working mechanism of light-driven out-of-plane rotation of micro/nanoscale rotors.

**a**, A simplified schematic illustrating the experimental setup and operation for OTER of micro/nanoparticles. **b**, Working mechanism of OTER: (i) In the non-uniform temperature field,  $\text{Na}^+$  and  $\text{Cl}^-$  ions, and polyethylene glycol (PEG) molecules diffuse to the cold region. Yellow arrows mark the discrete depletion forces ( $F_{Di}$ ) acting on the rotor, which lead to a total depletion force ( $F_D$ ) in (iv). (ii) A thermoelectric (TE) field is created by the separation  $\text{Na}^+$  and  $\text{Cl}^-$  ions owing to their different thermodiffusion coefficients. (iii) The temperature field also affects the dissociation of carboxylic function groups, thus the surface charges on the substrate. (iv) Optothermal forces and torque on the rotor: In the steady state, the gradient distribution of PEG molecules generates an attractive depletion force ( $F_D$ ) on the particle. A repulsive force ( $F_{TE}$ ) is generated from the TE field. A thermo-electrokinetic force ( $F_E$ ) is from the 11-Mercaptoundecanoic-acid-coated plasmonic substrate with non-uniform thermal-responsive surface charge (from -65 mV to -58 mV). The surface charge of the particle also varies with the temperature of the particle. For instance, the local surface charge of a carboxylic functionalized PS particle ranges from -55 mV to -49 mV. The “-” symbols indicate the temperature-dependent distributions of negative charges on the surface of the particle and substrate. The light-irradiated regimes with the higher temperature feature the lower charge density. A net torque,  $M_E$ , can be generated on the particle at certain position where a balance is reached among  $F_D$ ,  $F_{TE}$ , and  $F_E$ . The optical power is 78.4  $\mu\text{W}$ . The red dot marks the centroid of the particle.

## Characterizations and modelling of opto-thermoelectric rotation

To characterize and model the OTER, we start with a 2.8- $\mu\text{m}$  (in diameter) polystyrene (PS) particle with carboxylic functional groups as a rotor. The light-driven rotors allow us to characterize their rotation behavior *in situ* with optical microscopy. However, under the bright-field optical microscope, the rotation of the PS microparticle was barely observable (see Supplementary Movie 1) and the rotation rate could not be measured. To facilitate the optical characterization of the rotation behavior, we labelled the PS microparticle with two fluorescent nanobeads through streptavidin-biotin bonding (Fig. 2a(i)). Figure 2a(ii-vi) are the successive fluorescent images demonstrating the out-of-plane rotation of PS particle driven by a 660 nm laser at the power of 78.4  $\mu\text{W}$  in 5% PEG/5% PBS solution (also see Supplementary Movie 2). The variation in the position of the two nanobeads in the images reveals the orientation change of the PS particle due to the light-driven out-of-plane rotation. A detailed investigation of the rotation direction can be found in Supplementary Fig. 4. The fluorescence intensity of a pre-defined region encircling the rotor was measured over time for quantitative estimation of the rotation rate (Fig. 2b). The maximum fluorescence intensity was obtained when two nanobeads were simultaneously at the focal plane of the microscope. The fluorescence signal showed a periodic behavior corresponding to the rotation of the particle at an average rotation rate of 32.0 rpm. Different from conventional light-driven rotor systems where rotors are directly illuminated by laser beams<sup>37</sup>, the opto-thermoelectric rotors operate at a certain distance away from the laser beam. Such an off-axis rotation would protect delicate rotors such as live cells from the damage caused by high-power optical illumination. As illustrated in the insets of Fig. 2a (ii-vi), the particle-laser (PL) distance is around 2  $\mu\text{m}$ .

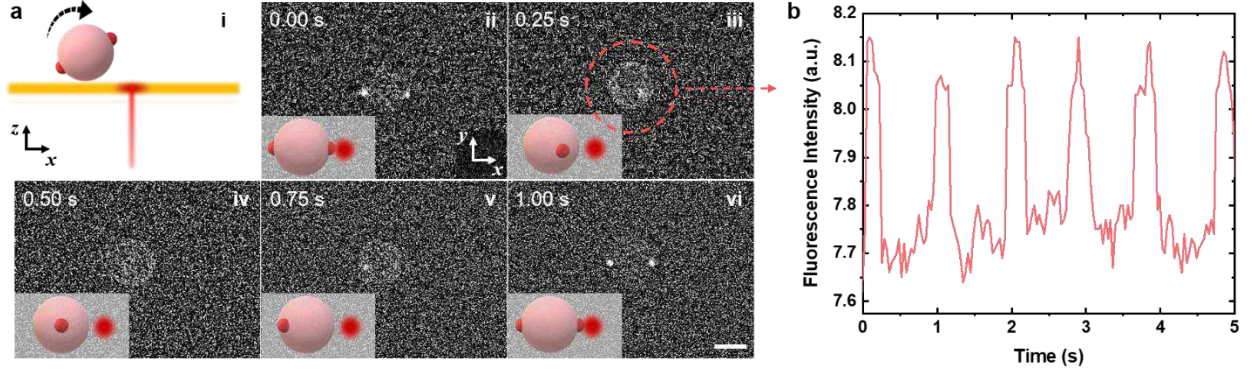


**Fig. 2** *In-situ* optical characterization of light-driven out-of-plane rotation of a spherical microparticle.

**a**, (i) Schematic illustration of the out-of-plane rotation of a spherical PS particle (i.e., rotor) around an axis parallel to the substrate. The driving laser beam, which propagates perpendicular to the substrate, heats the region of substrate near the particle. The particle is suspended in a 5% PEG/5% PBS solution covering the substrate. The two red beads are fluorescent nanoparticles for the visualization of the orientation change of the rotor under an epi-fluorescence microscope. The focal plane of the optical microscope is around 1  $\mu\text{m}$  above the substrate. (ii-vi) Successive fluorescence images of a rotating 2.8- $\mu\text{m}$  PS particle. Insets are schematic illustrations of the orientations of the rotor with two fluorescent nanoparticles as markers. Experimentally, two 40-nm (in diameter) fluorescent PS nanoparticles were attached to the rotor through streptavidin-biotin bonding. The red point on the right side of the rotor marks the position of the driving laser beam. Scale bar: 2  $\mu\text{m}$ . **b**, Time-dependent fluorescence intensity measured from the rotor and its surroundings as marked in **a**(iii). The out-of-plane rotation of the rotor leads to the periodic fluctuation of the fluorescence intensity. The intensity peaks appear when the rotation leads to both of fluorescent nanoparticles in the focal plane of the optical microscope.

To quantitatively analyze the working forces of OTER, we combined experimental measurements with finite element analysis (FEA), molecular dynamics (MD) and finite-difference time-domain (FDTD) simulations (see Methods and Supplementary Note 3 for simulation details). In the non-uniform temperature field, thermo-responsive charges on the rotor and substrate vary with the rotor location. Therefore, thermo-electrokinetic force acting on the rotor changes with PL distance, so does the torque on the rotor. We calculated the optothermal forces (i.e., depletion force, TE force, and thermo-electrokinetic force) and torques acted on the rotor as a function of PL distance. Depletion force is given as,

$$\mathbf{F}_D = - \oint c_{\text{PEG}} k_B T dA_r \hat{\mathbf{n}} \quad (1)$$

where  $c_{\text{PEG}}$  is the local concentration of PEG molecules,  $k_B$  is the Boltzmann constant,  $T$  is the local temperature,  $dA_r$  is the differential area element on the particle surface,  $\hat{\mathbf{n}}$  is unit vector normal to the rotor surface. TE force was obtained by the integration of parallel component of the thermoelectric field at the rotor surface:

$$\mathbf{F}_{\text{TE}} = \oint \sigma_r \mathbf{E}_{\text{TE},\parallel} dA_r \quad (2)$$

where  $\sigma_r$  is the surface charge density of the rotor measured from the zeta potential and  $\mathbf{E}_{TE,\parallel}$  is the tangential component of the thermoelectric field along the rotor. Thermo-electrokinetic force is expressed as,

$$\mathbf{F}_E = \oint \sigma_r dA_r \int_{x \rightarrow -\infty}^{x \rightarrow \infty} \int_{y \rightarrow -\infty}^{y \rightarrow \infty} \mathbf{E}_{\parallel} \quad (3)$$

where  $\mathbf{E}_{\parallel}$  is the parallel component of the electric field (which is generated by the substrate) on the rotor surface (see Supplementary Note 4).

Please note that we refer to forces passing through the centroid of the rotor when analyzing the forces along  $x$ ,  $y$ ,  $z$  direction (Fig. 1a). Originating from the thermo-diffusion of molecules and ions,  $\mathbf{F}_D$ , and  $\mathbf{F}_{TE}$  strongly depend on the temperature gradient in the solution (see Supplementary Note 4 for optothermal force analysis)<sup>38</sup>. Since the spatial distribution of temperature gradient is not uniform (Supplementary Fig. 5),  $\mathbf{F}_D$  and  $\mathbf{F}_{TE}$  along  $x$  axis vary with PL distance according to Eq. 1 and 2 (Fig. 3a). As shown in the inset of Fig. 3a, in PEG/PBS solutions,  $\mathbf{F}_D$  and  $\mathbf{F}_{TE}$  on a negatively charged PS particle have similar magnitude but opposite sign. The  $x$  component of the thermo-electrokinetic force,  $\mathbf{F}_E^x$ , is two orders of magnitude smaller than  $\mathbf{F}_D^x$  and  $\mathbf{F}_{TE}^x$  (see Supplementary Fig. 6a). Therefore,  $\mathbf{F}_D^x$  and  $\mathbf{F}_{TE}^x$  dominate the migration of the PS particle. We can see that a force balance reaches at the PL distance of 2.1  $\mu\text{m}$ , which is consistent with our measured PL distance (see Supplementary Fig. 7). Specifically, along  $x$  direction, the net force,  $\mathbf{F}^x = \mathbf{F}_D^x + \mathbf{F}_{TE}^x$ , equals to zero. Since the temperature field is symmetric about  $y$ -axis, all the corresponding forces along  $y$  direction are zero, i.e., the net force  $\mathbf{F}^y = \mathbf{F}_D^y = \mathbf{F}_{TE}^y = \mathbf{F}_E^y = 0$ . Along  $z$  directions, the net force  $\mathbf{F}^z = \mathbf{F}_D^z + \mathbf{F}_V^z + \mathbf{F}_G + \mathbf{F}_{TE}^z + \mathbf{F}_E^z + \mathbf{F}_B$ , where  $\mathbf{F}_V^z$  is Van der Waals force,  $\mathbf{F}_G$  is gravity, and  $\mathbf{F}_B$  is buoyant force. A net force of zero along  $z$  axis is obtained by the self-adapting gap (which is estimated as 30 nm) between the rotor and substrate. Specifically, the gap controls the depletion force  $\mathbf{F}_D^z$  and electrokinetic force  $\mathbf{F}_E^z$  acting on the rotor. The depletion force pushes the particle towards the substrate, which is balanced by the repulsive electrokinetic force at a suitable gap. We define the PL distance, where zero net force acts on the rotor (while the torque is non-zero), as a critical PL distance. The net torques on the PS particle at different PL distances were also calculated and shown in Fig. 3b. The hydrodynamic torque acting on a spherical particle rotating around an axis parallel to a planar boundary with a small sphere-wall gap is given by<sup>39,40</sup>,

$$M_d = \omega a^3 \nu \rho \phi(d);$$

$$\phi(d) = C \left( 0.4 \log \left( \frac{a}{a-d} \right) + 0.37 \right) \quad (4)$$

where  $\omega$  is the rotation rate,  $a$  is the radius of the particle,  $\nu$  is the kinematic viscosity of the solution,  $\rho$  is the density of the solution,  $\phi(d)$  is the correction factor of wall effect,  $d$  is the distance between rotor and the plane, and  $C$  is a constant. For a 2.8- $\mu\text{m}$  PS particle rotating at 35 rpm in the 5% PEG/5% PBS solution, we obtained a simulated thermo-electrokinetic torque of 1.6 pN·nm, which is close to the theoretical hydrodynamic torque, i.e., 1.09 pN·nm (Supplementary Note 5).

A series of control experiments and simulations were conducted to further investigate the roles of different forces in the rotor (see Supplementary Note 6 and Supplementary Movie 3 for details). The electrokinetic force arising from the thermo-responsive surface charge on the light-absorbing substrate functionalized with COOH-SAMs powers the rotation of the rotor, while the depletion

and TE forces arising from the thermophoresis of molecules and ions in the PEG/PBS solutions under the light-generated temperature gradient contribute to fixing the rotor in space for a steady rotation. Owing to the low optical power, the optical torque acting on the particle is too small to drive the rotation (Supplementary Fig. 8). Thermo-osmosis flow, which could rotate microparticles<sup>31,41</sup>, is negligible in our rotor because of the highly charged substrate and the thicker chamber in which our rotor is located<sup>42,43</sup>.

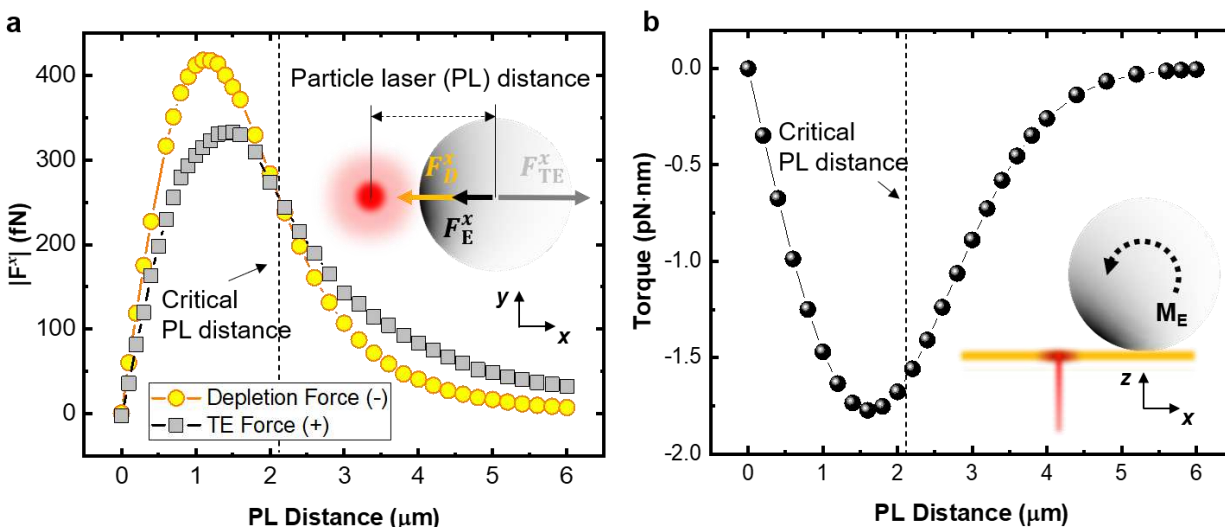


**Fig. 3 Quantitative analysis and modelling of opto-thermoelectric rotation of single spherical rotors.**

**a**, Simulated magnitudes of depletion force and TE force along  $x$  axis on a 2.8- $\mu\text{m}$  PS particle as a function of PL distance in a 5% PEG/5% PBS solution. As marked by the dash line, a balance between depletion force and TE force (i.e., zero net force) is reached at a critical PL distance of 2.1  $\mu\text{m}$ . Inset: Schematic illustration of force analysis for the light-driven rotor in the  $xy$  plane. The red and white circles represent the laser spot and the rotor, respectively. **b**, Simulated torque ( $M_E$ ) acting on the rotor as a function of PL distance. The torque at the critical PL distance (2.1  $\mu\text{m}$ ) is around -1.6 pN·nm.

### On-demand control of rotation behaviors

We further studied the effects of solute concentration, laser power and particle property on the rotation behavior and devised the on-demand control of OTER. To study the roles of PEG molecules in the rotation behaviors of rotors, we measured the rotation rate of a 2.8- $\mu\text{m}$  PS particle in 5% PBS solutions with variable PEG concentrations in the range of 5% - 15%. The amount of PEG molecules does not influence the thermo-electrokinetic force or the torque on the rotor. However, the higher PEG concentration increases the viscosity of the solution<sup>44</sup> and strengthens the depletion force. As a result, the rotation rate at an optical power of 196  $\mu\text{W}$  decreases from 84.1 rpm to 30.9 rpm when PEG concentration increases from 5% to 15% (Fig. 4a). Such a variation in the rotation rate matches well with the theoretically predicted values obtained from Eq. 4 (see Supplementary Note 5 for details). Meanwhile, the critical PL distance shifts from 2.1 to 2.9  $\mu\text{m}$  in order to reach a new balance between the enhanced depletion force and the constant TE force. To evaluate the dependence of rotation on the PBS concentration, we measured the rotation rate of the PS particle in solutions with the different PBS concentrations, as summarized

in Fig. 4b. The surface charge densities of the particle and substrate increase with the PBS concentration according to Gouy–Chapman theory<sup>45</sup>. However, the increased ionic strength at the higher PBS concentration enhances the Debye screening effect and reduces the zeta potential of the particle in the solution, which weakens the thermo-electrokinetic force according to Eq. 3. Therefore, the rotation rate decreases when the PBS concentration increases from 5% to 15%. Due to the non-linear dependence of the charge densities on the ionic strength<sup>46</sup>, the reduction in rotation rate is larger when the PBS concentration increases from 5% to 10% than that from 10% to 15%. The change in TE force is negligible due to a tradeoff between the enhanced TE field and the decreased zeta potential<sup>32</sup>.

We can also control the rotation behavior by tuning the optical power of the driving laser beam. As shown in Fig. 4b, the rotation rate increases linearly with optical power. The linear behavior arises from the linear dependence of the temperature gradient and thus the magnitude of thermo-electrokinetic force on the optical power (Supplementary Fig. 6b). However, the maximum rotation rate is limited by a maximum optical power beyond which the optical heating of the substrate would generate a vapor bubble<sup>47</sup>. The bubble generation would lead to a strong Marangoni flow that transports the rotor to the bubble at a velocity of several meters per second, resulting in the printing of the rotor on the substrate<sup>48,49</sup>. A maximum rotation rate of 267 rpm was achieved for the 2.8- $\mu\text{m}$  PS particle at an optical power of  $\sim 630 \mu\text{W}$ .

To explore the size effects on the rotation behavior, we measured and simulated rotation rates of spherical particles, along with torques acting on the particles, as a function of the particle size, as shown in Fig. 4c. Approximately, the magnitude of calculated torque (see Supplementary Note 5) increases linearly with the particle size. The negative torque indicates that the rotation direction is anticlockwise as shown in the inset of Fig. 4d. The increased torque for the larger particle arises from the increased thermo-electrokinetic force, which is related to the enlarged particle surface and the reduced gradient of surface charge on the particle. The temperature gradient at particle center decreases from 10.1 to 1.6 K/ $\mu\text{m}$  when the particle size increases from 300 nm to 2.8  $\mu\text{m}$  (see Supplementary Fig. 9a). The decreased temperature gradient is due to the increased distance between the larger particle and the laser beam (i.e., critical PL distance increases from 0.47  $\mu\text{m}$  to 2.1  $\mu\text{m}$ ) as shown in Supplementary Fig. 9b-d. We further simulated the rotation rates (red circle) of the particles by substituting the simulated torques into to Eq. 4, which match well the measured rotation rates (red diamond). We can see that the rotation rate rises sharply as the particle size decreases from 2.8 to 0.3  $\mu\text{m}$ , mainly because the mass of the particle decreases with the cubic of its diameter.

The zeta potential of rotors can also be employed to control the rotational behavior. We studied the light-driven rotation of 1- $\mu\text{m}$  PS particles with different zeta potentials of -23, -38, and -47 mV (see Methods for preparation of the particles). As shown in Fig. 4d, a steady rotation was observed for the PS particle with the highest zeta potential (-47 mV). The critical PL distance was  $\sim 1 \mu\text{m}$ . However, upon the incidence of the laser beam onto the substrate near the particle, the particle with the zeta potential of -38 mV rolled toward the hot region and got trapped at the center of the laser beam (Supplementary Movie 4). The particle with the weakest zeta potential (-23 mV) underwent a sequence of light-driven events involving rolling, trapping and printing onto the substrate (also see Supplementary Movie 5). Figure 4d also shows the calculated net forces on the particles along  $x$  axis. For all the calculations in the figure, the PL distance was set at 1  $\mu\text{m}$ . The net force decreases from 0 to -47.7 fN when the zeta potential of the particle increases. The

negative net forces stem from the increased attractive depletion force and the decreased repulsive TE force acting on the particles with the weak zeta potentials (Supplementary Fig. 9d).

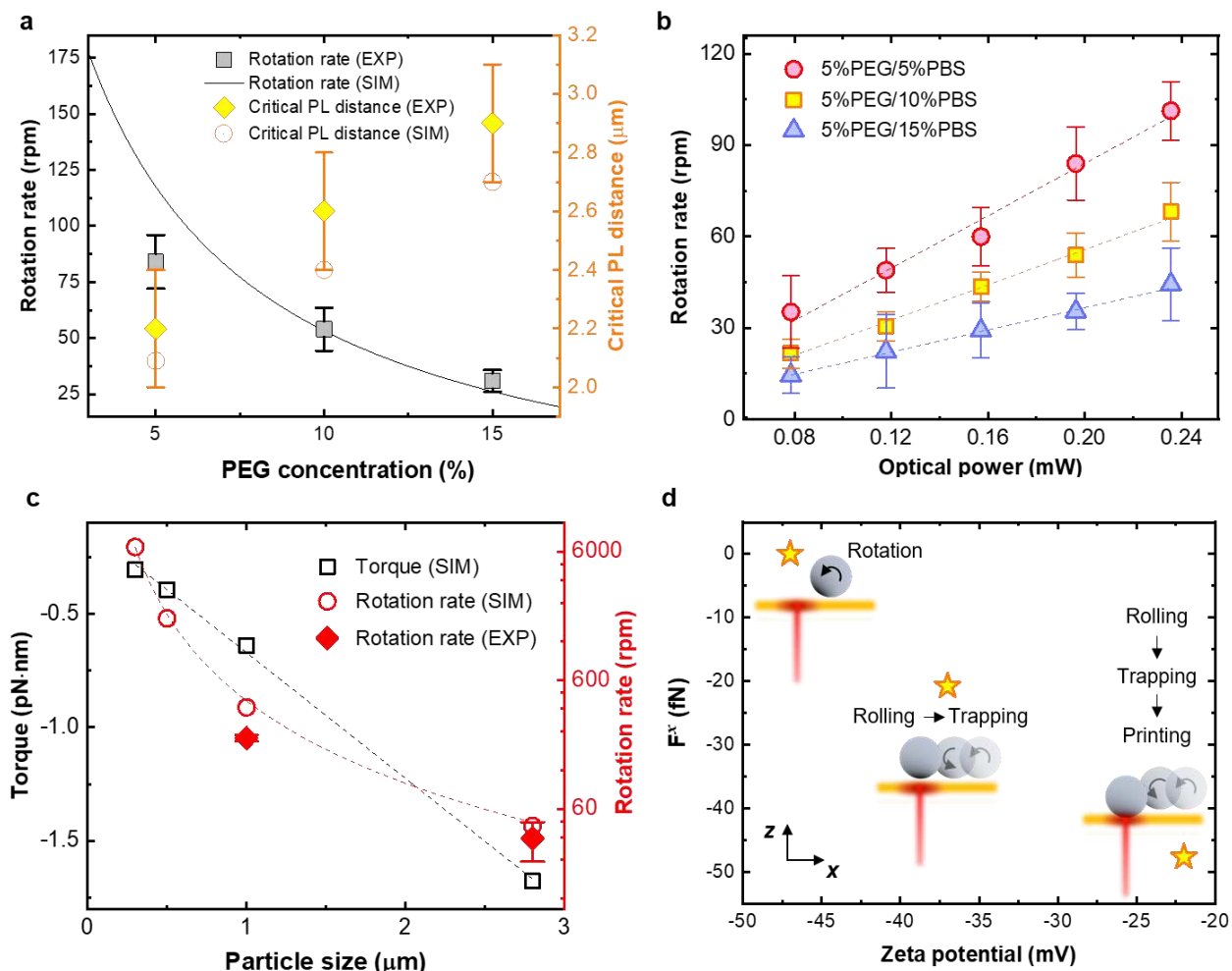


**Fig. 4 Parametric study and on-demand control of rotation behaviors.**

**a**, Rotation rate and critical PL distance of a 2.8- $\mu\text{m}$  PS particle versus PEG concentration in 5% PBS solutions at an optical power of 196  $\mu\text{W}$ . The grey squares and black line are experimentally measured (indicated as “EXP”) and simulated (indicated as “SIM”) rotation rates, respectively. The yellow diamonds and circles are measured and simulated critical PL distances, respectively. **b**, Measured rotation rate of the PS particle in 5% PEG solutions with different PBS concentrations versus the optical power of laser beam. The dashed lines are linear fittings of the measured values. **c**, Measured and simulated torque and rotation rate as a function of particle size in a 5% PEG/5% PBS solution. The black dash line is linear fitting of the simulated torques. The red dashed line is the inverse cubic fitting of the simulated rotation rate. **d**, Simulated net forces along  $x$  axis of 1- $\mu\text{m}$  PS particles with different zeta potentials of -23, -38, and -47 mV in a 15% PEG/5% PBS solution, which lead to the different behaviors of the particles as illustrated in the insets.

## General applicability of opto-thermoelectric rotation

We have demonstrated the general applicability of OTER to biological cells and synthetic particles of diverse materials, sizes, and shapes. Figure 5a displays the time-lapsed fluorescence images, showing the out-of-plane rotation of a 1- $\mu\text{m}$  PS spherical particle labelled by two fluorescent nanobeads (also see Supplementary Movie 6). The rotation rate was measured as 66.6 rpm at an optical power of 15.7  $\mu\text{W}$ . Rotation of a 500 nm PS/Au Janus particle (see Method for the particle preparation) with a rate of 163.8 rpm in a 15% PEG/5% PBS solution was demonstrated at the optical power of 9.4  $\mu\text{W}$  (Fig. 5b and Supplementary Movie 7).

When the rotors become smaller, it becomes challenging to visualize their rotation with conventional optical microscopy. To demonstrate the rotation of a 300 nm PS/Au Janus particle, we employed dark-field optical microscopy to monitor the variation in the scattered light from the rotating Janus particle (Fig. 5c and Supplementary Movie 8). To further quantify the rotation, we extracted the real-time red-green-blue (RGB) signals from the scattered light of the particle. As shown in the Fig. 5d, the magnitude of green and red signals varied periodically with a period of  $\sim 0.17$  s. The variations in the RGB signals correspond to the orientation change of the Janus particle due to the light-driven rotation (Supplementary Fig. 10). From Fig. 5d, we calculated the rotation rate of the Janus nanoparticle as  $\sim 353$  rpm.

OTER is also applicable to live cells (Supplementary Fig. 5e-f). Due to a large amount of ionized carboxyl and phosphoric acid groups on their surfaces, yeast cells have high negative zeta potential<sup>50</sup>. As shown in Fig. 5e, a yeast cell rotated at a high rate of  $\sim 300$  rpm at an optical power of 78.5  $\mu\text{W}$  (also see Supplementary Movie 9). Besides the spherical particles, rotation of quasi-one-dimensional *Bacillus subtilis* (*B. subtilis*) with a high aspect ratio of 8 has also been achieved (Fig. 5f). Due to the much smaller cross section ( $\sim 0.25$   $\mu\text{m}$  in diameter) of *B. subtilis*, the thermo-electrokinetic force on *B. subtilis* is weaker than that on yeast cells. As a result, the rotation rate of *B. subtilis* was around  $\sim 31.8$  rpm, which is about 1/10 of the rate of the yeast cell (see Supplementary Movie 10).

Moreover, OTER is applicable to rotors with the more complex architectures. As an example, we demonstrated the out-of-plane rotation of particle dimers, trimers, and hexamers. Figure 5g are the successive optical images showing the real-time rotation of a dimer composed of two 2- $\mu\text{m}$  silica particles (see Supplementary Movie 11). The rotation of a trimer composed of three 1- $\mu\text{m}$  PS particles and a hexamer composed of six 2- $\mu\text{m}$  silica particles are shown in Fig. 5h (also see Supplementary Movie 12) and Supplementary Fig. 11 (also see Supplementary Movie 13), respectively. It is worth noting that OTER enables an accurate control of the rotation angle, rotation axis and thus rotor orientation by controlling the power, duration, and position of the driving laser beam, facilitating its application in 3D profiling of biological cells and synthetic particles with high-resolution and time-consuming imaging techniques. As shown in Fig. 5g, the long axis of silica dimer remained perpendicular to the substrate when the laser beam was turned off after the dimer rotation for 1 s. We also demonstrated the precise rotation of a yeast cell along specific rotation axes for targeted angular degrees in order to reach any desired orientations (see Supplementary Fig. 12 and Supplementary Movie 14).

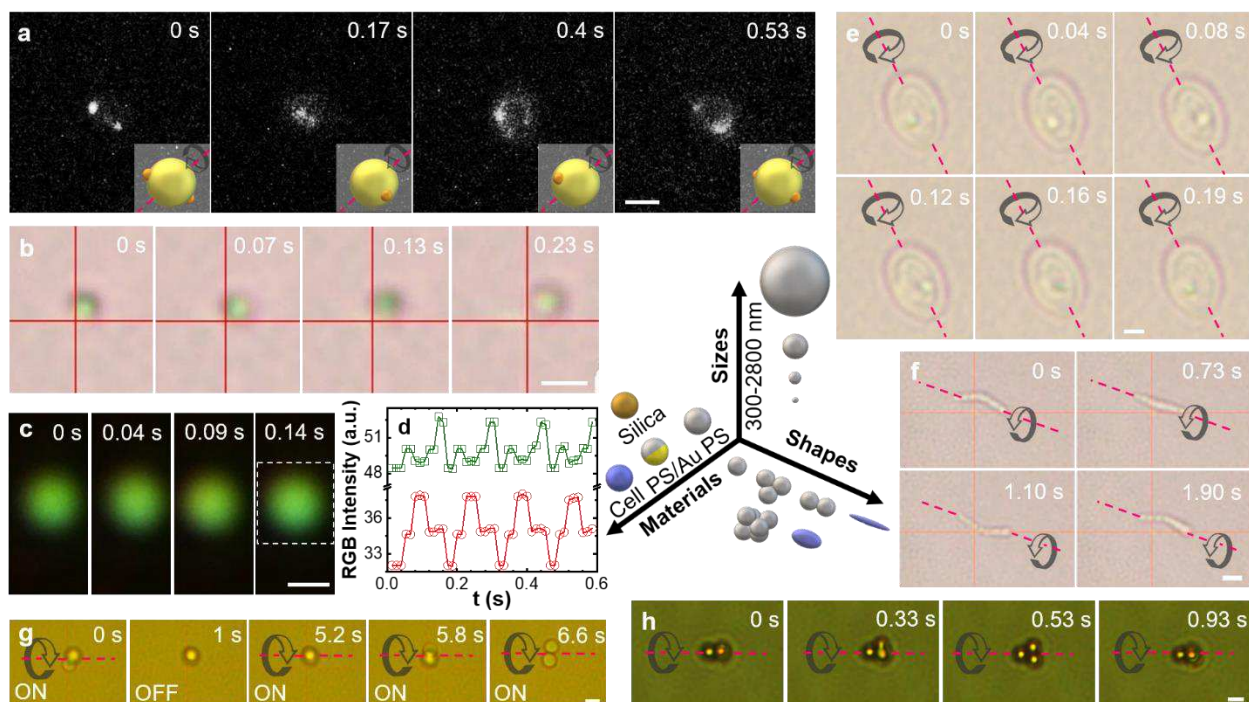


**Fig. 5 General applicability of opto-thermoelectric rotation to a variety of rotors with diverse shapes, sizes, and materials.**

**a**, Successive fluorescence images of a rotating 1- $\mu\text{m}$  PS particle labelled by fluorescent nanoparticles for the rotation visualization. **b**, Successive optical images of a rotating 500 nm PS/Au Janus particle. **c**, Successive dark-field optical images of a rotating 300 nm PS/Au Janus particle. **d**, Real-time RGB intensity of the dark-field optical images of the Janus particle. The white dash rectangle in **c** marks the selected area from which the RGB intensity is recorded. **e**, Successive optical images of a rotating yeast cell. **f**, Successive optical images of a rotating *B. subtilis*. **g**, Successive optical images of a rotating dimer composed of two 2- $\mu\text{m}$  silica particles. “ON” and “OFF” indicate that the laser beam is turned on and off, respectively. **h**, Successive optical images of a rotating trimer composed of three 1- $\mu\text{m}$  PS particles. The dash lines and black arrows represent the rotation axes and directions, respectively. Scale bars: **a, b, e, f, h**, 1  $\mu\text{m}$ ; **c**, 500 nm; **g**, 2  $\mu\text{m}$ . Solutions: **a-c, g-h**, 15% PEG/5% PBS; **e-f**, 5% PEG/5% PBS.

## Conclusion

By harnessing thermo-diffusion of ions and molecules in solutions and thermo-responsive charge at solid/liquid interfaces under the light-generated temperature gradient, we have developed OTER of arbitrary micro/nanoscale objects in liquid environment with simple and low-power optics. In contrast to previously demonstrated rotors that required laser beams with designed intensity profile and polarization, or rotors with sophisticated shapes or material birefringence, OTER enables the out-of-plane rotation of spherically symmetric and isotropic particles using a simple, low-power and linearly polarized Gaussian laser beam. As a general platform, OTER is applicable to diverse biological cells and synthetic particles of variable compositions, sizes and shapes. On-demand control of the rotation behaviors can be achieved by tuning the solutes or laser beam. Different from the conventional on-axis high-power (5–50 mW) rotors systems<sup>37</sup>, OTER enables off-axis rotation with a low-power (down to 9.4  $\mu\text{W}$ ) laser beam, holding great promise for a non-invasive 3D cellular analysis. With its superior performances, universal applicability, and simple optics,

OTER of micro/nanoscale objects will find a wide range of applications in sensing, imaging, biomedicine, and manufacturing.

## References

- 1 Ahn, J. *et al.* Ultrasensitive torque detection with an optically levitated nanorotor. *Nat. Nanotechnol.* **15**, 89-93, doi:10.1038/s41565-019-0605-9 (2020).
- 2 Soong, R. K. *et al.* Powering an inorganic nanodevice with a biomolecular motor. *Science* **290**, 1555-1558, doi:10.1126/science.290.5496.1555 (2000).
- 3 Nelson, B. J., Kaliakatsos, I. K. & Abbott, J. J. Microrobots for minimally invasive medicine. *Annu. Rev. Biomed. Eng.* **12**, 55-85, doi:10.1146/annurev-bioeng-010510-103409 (2010).
- 4 Butaite, U. G. *et al.* Indirect optical trapping using light driven micro-rotors for reconfigurable hydrodynamic manipulation. *Nat. Commun.* **10**, 1215, doi:10.1038/s41467-019-08968-7 (2019).
- 5 Grier, D. G. A revolution in optical manipulation. *Nature* **424**, 810-816, doi:10.1038/nature01935 (2003).
- 6 Qian, B., Montiel, D., Bregulla, A., Cichos, F. & Yang, H. Harnessing thermal fluctuations for purposeful activities: the manipulation of single micro-swimmers by adaptive photon nudging. *Chem. Sci.* **4**, 1420-1429, doi:10.1039/c2sc21263c (2013).
- 7 Ahn, J. *et al.* Optically Levitated Nanodumbbell Torsion Balance and GHz Nanomechanical Rotor. *Phys. Rev. Lett.* **121**, 033603, doi:10.1103/PhysRevLett.121.033603 (2018).
- 8 Tamura, M., Omatsu, T., Tokonami, S. & Iida, T. Interparticle-Interaction-Mediated Anomalous Acceleration of Nanoparticles under Light-Field with Coupled Orbital and Spin Angular Momentum. *Nano Lett.* **19**, 4873-4878, doi:10.1021/acs.nanolett.9b00332 (2019).
- 9 Donato, M. G. *et al.* Optical Trapping, Optical Binding, and Rotational Dynamics of Silicon Nanowires in Counter-Propagating Beams. *Nano Lett.* **19**, 342-352, doi:10.1021/acs.nanolett.8b03978 (2019).
- 10 Kreysing, M. *et al.* Dynamic operation of optical fibres beyond the single-mode regime facilitates the orientation of biological cells. *Nat. Commun.* **5**, 5481, doi:10.1038/ncomms6481 (2014).
- 11 Forrester, A., Courtial, J. & Padgett, M. J. Performance of a rotating aperture for spinning and orienting objects in optical tweezers. *J. Mod. Opt.* **50**, 1533-1538, doi:10.1080/09500340308235227 (2003).
- 12 Paterson, L. *et al.* Controlled Rotation of Optically Trapped Microscopic Particles. *Science* **292**, 912-914, doi:10.1126/science.1058591 %J Science (2001).
- 13 Shao, L., Yang, Z. J., Andren, D., Johansson, P. & Kall, M. Gold Nanorod Rotary Motors Driven by Resonant Light Scattering. *ACS Nano* **9**, 12542-12551, doi:10.1021/acs.nano.5b06311 (2015).
- 14 Padgett, M. & Bowman, R. Tweezers with a twist. *Nat. Photonics* **5**, 343-348, doi:10.1038/nphoton.2011.81 (2011).
- 15 Han, F. *et al.* Crossover from positive to negative optical torque in mesoscale optical matter. *Nat. Commun.* **9**, 4897, doi:10.1038/s41467-018-07376-7 (2018).

- 16 Reimann, R. *et al.* GHz Rotation of an Optically Trapped Nanoparticle in Vacuum. *Phys. Rev. Lett.* **121**, 033602, doi:10.1103/PhysRevLett.121.033602 (2018).
- 17 Zong, Y. *et al.* An Optically Driven Bistable Janus Rotor with Patterned Metal Coatings. *ACS Nano* **9**, 10844-10851, doi:10.1021/acsnano.5b03565 (2015).
- 18 Nan, F. & Yan, Z. Synergy of Intensity, Phase, and Polarization Enables Versatile Optical Nanomanipulation. *Nano Lett.* **20**, 2778-2783, doi:10.1021/acs.nanolett.0c00443 (2020).
- 19 Asavei, T. *et al.* Optically trapped and driven paddle-wheel. *New J. Phys.* **15**, 063016, doi:10.1088/1367-2630/15/6/063016 (2013).
- 20 Vizsnyiczai, G. *et al.* Multiview microscopy of single cells through microstructure-based indirect optical manipulation. *Biomed. Opt. Express* **11**, 945-962, doi:10.1364/BOE.379233 (2020).
- 21 Ashkin, A., Dziedzic, J. M., Bjorkholm, J. E. & Chu, S. Observation of a single-beam gradient force optical trap for dielectric particles. *Opt. Lett.* **11**, 288-290, doi:10.1364/OL.11.000288 (1986).
- 22 Tachibana, M. *et al.* Human Embryonic Stem Cells Derived by Somatic Cell Nuclear Transfer. *Cell* **153**, 1228-1238, doi:<https://doi.org/10.1016/j.cell.2013.05.006> (2013).
- 23 Habaza, M. *et al.* Rapid 3D Refractive-Index Imaging of Live Cells in Suspension without Labeling Using Dielectrophoretic Cell Rotation. *Adv. Sci.* **4**, 1600205, doi:10.1002/advs.201600205 (2017).
- 24 Huang, L., Zhao, P., Liang, F. & Wang, W. Single-cell 3D electro-rotation. *Methods Cell Biol.* **148**, 97-116, doi:10.1016/bs.mcb.2018.06.013 (2018).
- 25 Ding, X. *et al.* On-chip manipulation of single microparticles, cells, and organisms using surface acoustic waves. *Proc. Natl. Acad. Sci. U. S. A.* **109**, 11105-11109, doi:10.1073/pnas.1209288109 (2012).
- 26 Ahmed, D. *et al.* Rotational manipulation of single cells and organisms using acoustic waves. *Nat. Commun.* **7**, 11085, doi:10.1038/ncomms11085 (2016).
- 27 Jeon, S. *et al.* Magnetically actuated microrobots as a platform for stem cell transplantation. *Sci. Robot.* **4**, eaav4317, doi:10.1126/scirobotics.aav4317 (2019).
- 28 Ahmed, D. *et al.* Neutrophil-inspired propulsion in a combined acoustic and magnetic field. *Nat. Commun.* **8**, 770, doi:10.1038/s41467-017-00845-5 (2017).
- 29 Kolb, T., Albert, S., Haug, M. & Whyte, G. Optofluidic rotation of living cells for single-cell tomography. *J. Biophotonics* **8**, 239-246, doi:10.1002/jbio.201300196 (2015).
- 30 Liang, W. *et al.* Label-free characterization of different kinds of cells using optoelectrokinetic-based microfluidics. *Opt. Lett.* **45**, 2454-2457, doi:10.1364/OL.384883 (2020).
- 31 Lou, X., Yu, N., Liu, R., Chen, K. & Yang, M. Dynamics of a colloidal particle near a thermoosmotic wall under illumination. *Soft Matter* **14**, 1319-1326, doi:10.1039/c7sm02196h (2018).
- 32 Ding, H., Kollipara, P. S., Lin, L. & Zheng, Y. Atomistic modeling and rational design of optothermal tweezers for targeted applications. *Nano Research* **14**, 295-303, doi:10.1007/s12274-020-3087-z (2020).
- 33 Jiang, H. R., Wada, H., Yoshinaga, N. & Sano, M. Manipulation of colloids by a nonequilibrium depletion force in a temperature gradient. *Phys. Rev. Lett.* **102**, 208301, doi:10.1103/PhysRevLett.102.208301 (2009).

- 34 Maeda, Y. T., Tlusty, T. & Libchaber, A. Effects of long DNA folding and small RNA stem-loop in thermophoresis. *Proc. Natl. Acad. Sci. U. S. A.* **109**, 17972-17977, doi:10.1073/pnas.1215764109 (2012).
- 35 Atkins, P. & de Paula, J. *Physical Chemistry*. 8th edn, (Oxford University Press, 2006).
- 36 Blandamer, M. J., Burgess, J., Duce, P. P., Robertson, R. E. & Scott, J. W. M. Analysis of the dependence on temperature of the acid dissociation constants for mono-carboxylic acids in water in terms of a two-stage mechanism. *J. Chem. Soc., Faraday Trans.1* **77**, 2281-2286, doi:10.1039/f19817702281 (1981).
- 37 Shao, L. & Käll, M. Light-Driven Rotation of Plasmonic Nanomotors. *Adv. Funct. Mater.* **28**, 1706272, doi:10.1002/adfm.201706272 (2018).
- 38 Kollipara, P. S., Lin, L. & Zheng, Y. Thermo-Electro-Mechanics at Individual Particles in Complex Colloidal Systems. *J. Phys. Chem. C* **123**, 21639-21644, doi:10.1021/acs.jpcc.9b06425 (2019).
- 39 Liu, Q. & Prosperetti, A. Wall effects on a rotating sphere. *J. Fluid Mech.* **657**, 1-21, doi:10.1017/s002211201000128x (2010).
- 40 Goldman, A. J., Cox, R. G. & Brenner, H. Slow viscous motion of a sphere parallel to a plane wall—I Motion through a quiescent fluid. *Chem. Eng. Sci.* **22**, 637-651, doi:10.1016/0009-2509(67)80047-2 (1967).
- 41 Heidari, M., Bregulla, A., Muinos Landin, S., Cichos, F. & von Klitzing, R. Self-propulsion of Janus particles near a brush-functionalized substrate. *Langmuir*, 7775–7780, doi:10.1021/acs.langmuir.0c00461 (2020).
- 42 Bregulla, A. P., Wurger, A., Gunther, K., Mertig, M. & Cichos, F. Thermo-Osmotic Flow in Thin Films. *Phys. Rev. Lett.* **116**, 188303, doi:10.1103/PhysRevLett.116.188303 (2016).
- 43 Gargiulo, J. *et al.* Understanding and Reducing Photothermal Forces for the Fabrication of Au Nanoparticle Dimers by Optical Printing. *Nano Lett.* **17**, 5747-5755, doi:10.1021/acs.nanolett.7b02713 (2017).
- 44 Ninni, L., Burd, H., Fung, W. H. & Meirelles, A. J. A. Kinematic Viscosities of Poly(ethylene glycol) Aqueous Solutions. *J. Chem. Eng. Data* **48**, 324-329, doi:10.1021/je0255731 (2003).
- 45 Ohsawa, K., Murata, M. & Ohshima, H. Zeta potential and surface charge density of polystyrene-latex; comparison with synaptic vesicle and brush border membrane vesicle. *Colloid Polym. Sci.* **264**, 1005-1009, doi:10.1007/bf01410317 (1986).
- 46 Zhu, S., Panne, U. & Rurack, K. A rapid method for the assessment of the surface group density of carboxylic acid-functionalized polystyrene microparticles. *Analyst* **138**, 2924-2930, doi:10.1039/c3an36578f (2013).
- 47 Lee, E., Huang, D. & Luo, T. Ballistic supercavitating nanoparticles driven by single Gaussian beam optical pushing and pulling forces. *Nat. Commun.* **11**, 2404, doi:10.1038/s41467-020-16267-9 (2020).
- 48 Lin, L. *et al.* Bubble-Pen Lithography. *Nano Lett.* **16**, 701-708, doi:10.1021/acs.nanolett.5b04524 (2016).
- 49 Zhao, C. *et al.* Theory and experiment on particle trapping and manipulation via optothermally generated bubbles. *Lab Chip* **14**, 384-391, doi:10.1039/c3lc50748c (2014).
- 50 Tazhibaeva, S. M., Musabekov, K. B., Orazymbetova, A. B. & Zhubanova, A. A. Surface Properties of Yeast Cells. *Colloid J.* **65**, 122-124, doi:10.1023/a:1022391613491 (2003).

## **Acknowledgments**

Y.Z. work was supported by the National Science Foundation (NSF-ECCS-2001650), the National Aeronautics and Space Administration (80NSSC17K0520), and the National Institute of General Medical Sciences of the National Institutes of Health (DP2GM128446). We thank the Texas Advanced Computing Centre (TACC) at The University of Texas at Austin for providing HPC resources that contributed to the research results reported within this paper. URL: <http://www.tacc.utexas.edu>. We also thank Kan Yao, Yaoran Liu, Jingang Li, and Youngsun Kim for the assistance in experiments.

## **Author contributions**

H.D. and Y.Z. conceived the idea for this study. H.D. prepared materials and worked on the experiments. P.K. and H.D. conducted the simulations. Y.Z. supervised the project. All authors discussed the results and wrote the manuscript.

## **Competing interests**

Authors have no competing interests.

## **Additional information**

**Supplementary information** is available for this paper at <https://doi.org/xxxx>.

**Reprints and permissions information** is available at [www.nature.com/reprints](http://www.nature.com/reprints).

**Correspondence and requests for materials** should be addressed to Y.Z.

# Figures

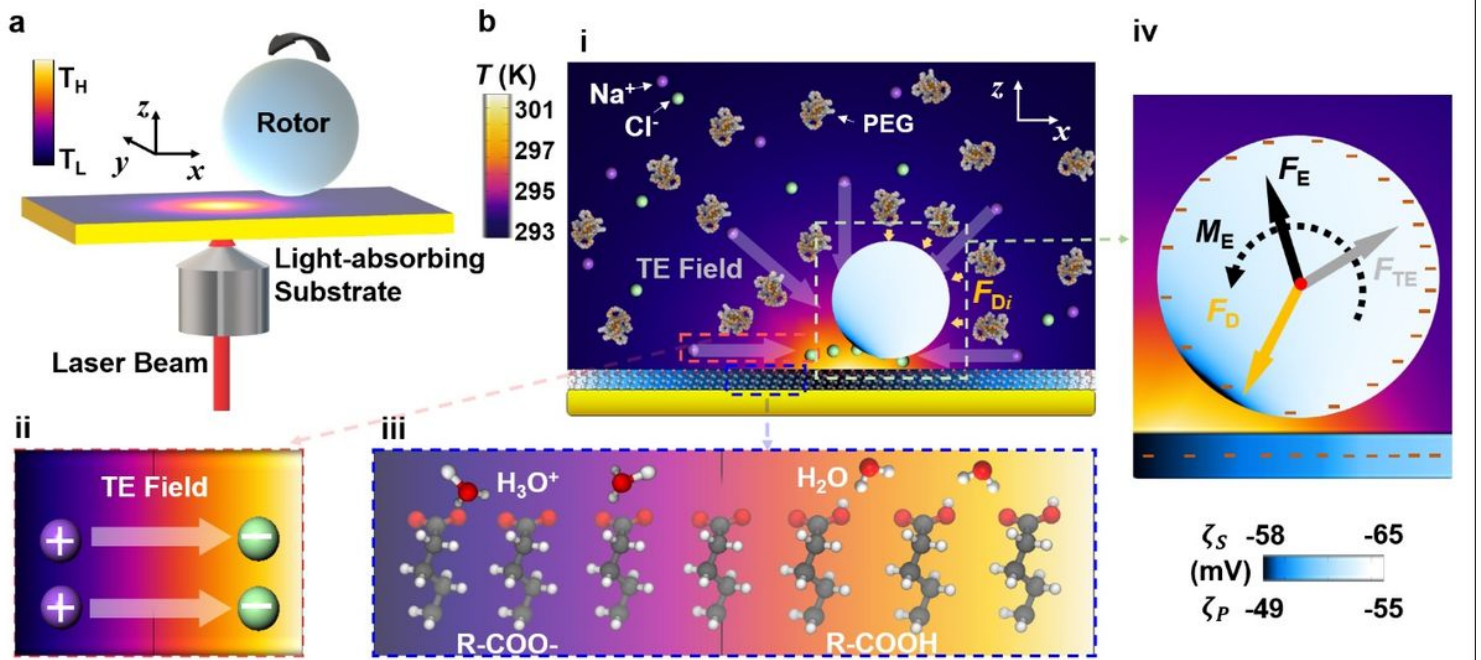
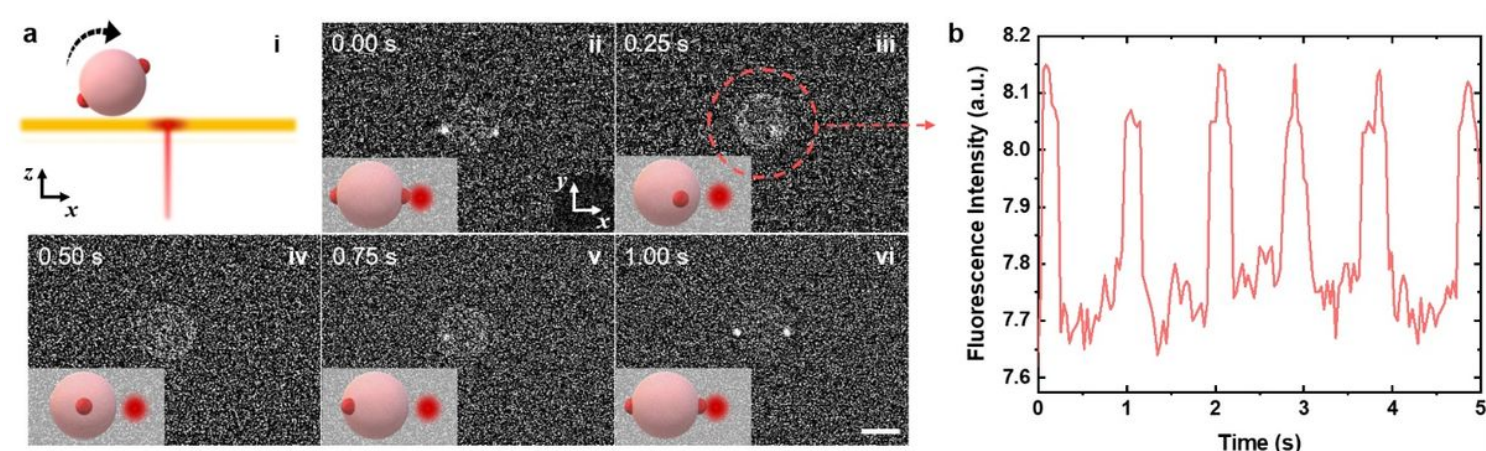


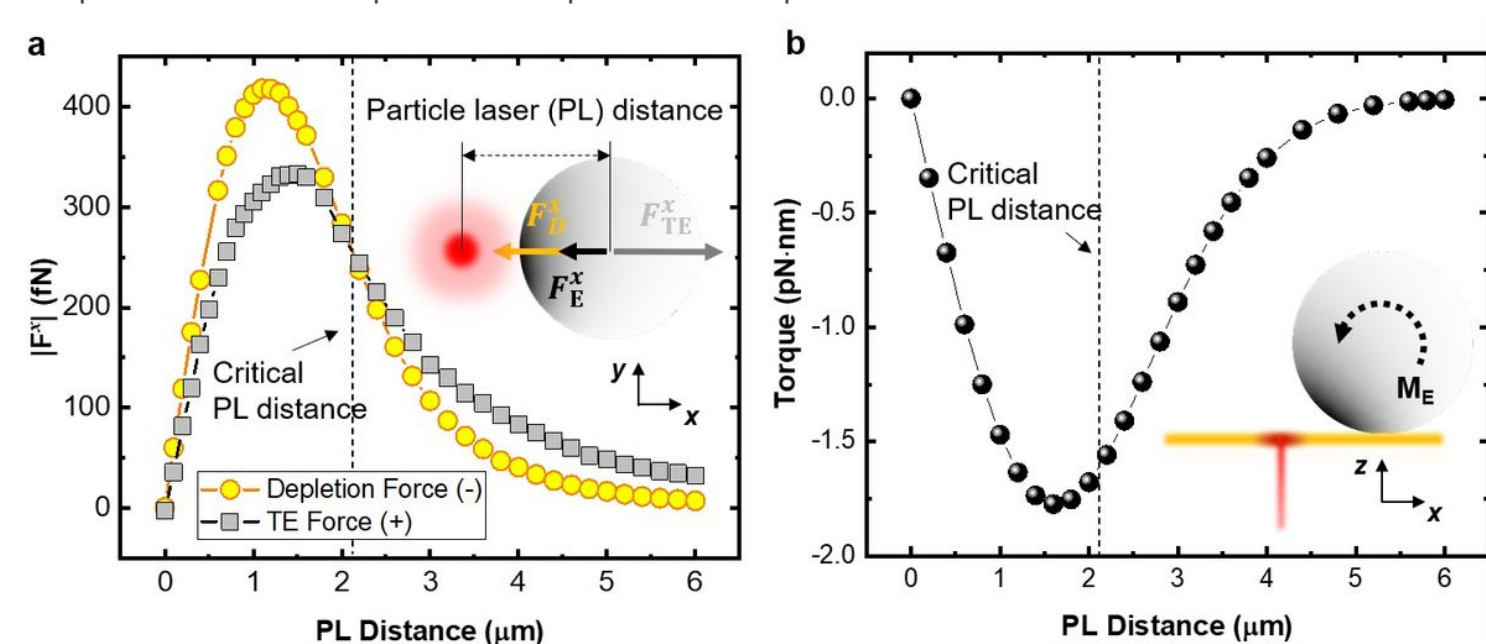
Figure 1

Working mechanism of light-driven out-of-plane rotation of micro/nanoscale rotors. a, A simplified schematic illustrating the experimental setup and operation for OTER of micro/nanoparticles. b, Working mechanism of OTER: (i) In the non-uniform temperature field,  $\text{Na}^+$  and  $\text{Cl}^-$  ions, and polyethylene glycol (PEG) molecules diffuse to the cold region. Yellow arrows mark the discrete depletion forces ( $F_{Di}$ ) acting on the rotor, which lead to a total depletion force ( $F_D$ ) in (iv). (ii) A thermoelectric (TE) field is created by the separation  $\text{Na}^+$  and  $\text{Cl}^-$  ions owing to their different thermodiffusion coefficients. (iii) The temperature field also affects the dissociation of carboxylic function groups, thus the surface charges on the substrate. (iv) Optothermal forces and torque on the rotor: In the steady state, the gradient distribution of PEG molecules generates an attractive depletion force ( $F_D$ ) on the particle. A repulsive force ( $F_{TE}$ ) is generated from the TE field. A thermo-electrokinetic force ( $F_E$ ) is from the 11-Mercaptoundecanoic-acid-coated plasmonic substrate with non-uniform thermal-responsive surface charge (from -65 mV to -58 mV). The surface charge of the particle also varies with the temperature of the particle. For instance, the local surface charge of a carboxylic functionalized PS particle ranges from -55 mV to -49 mV. The  $\zeta$  symbols indicate the temperature-dependent distributions of negative charges on the surface of the particle and substrate. The light-irradiated regimes with the higher temperature feature the lower charge density. A net torque,  $M_E$ , can be generated on the particle at certain position where a balance is reached among  $F_D$ ,  $F_{TE}$ , and  $F_E$ . The optical power is 78.4  $\mu\text{W}$ . The red dot marks the centroid of the particle.



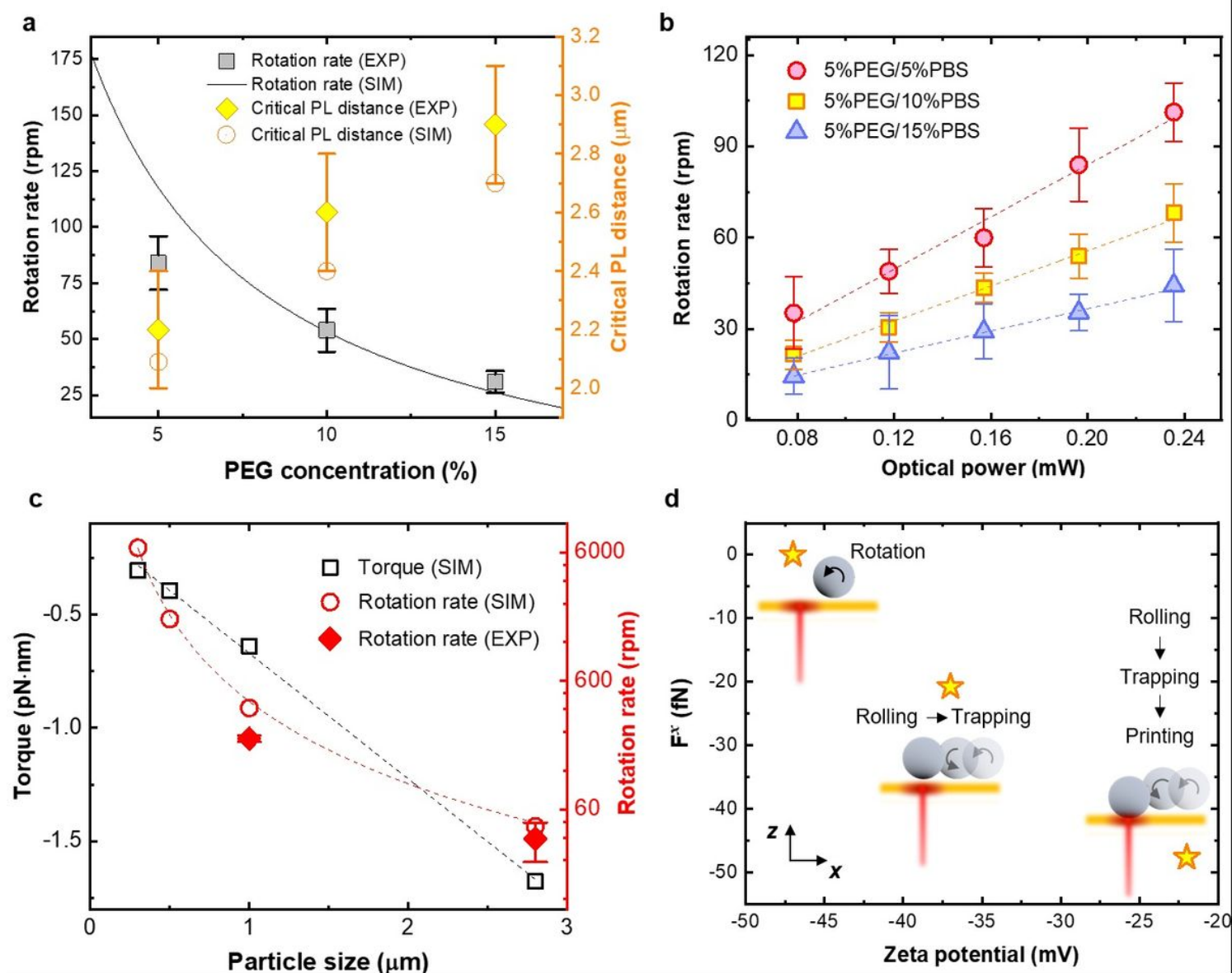
**Figure 2**

In-situ optical characterization of light-driven out-of-plane rotation of a spherical microparticle. a, (i) Schematic illustration of the out-of-plane rotation of a spherical PS particle (i.e., rotor) around an axis parallel to the substrate. The driving laser beam, which propagates perpendicular to the substrate, heats the region of substrate near the particle. The particle is suspended in a 5% PEG/5% PBS solution covering the substrate. The two red beads are fluorescent nanoparticles for the visualization of the orientation change of the rotor under an epi-fluorescence microscope. The focal plane of the optical microscope is around  $1\ \mu\text{m}$  above the substrate. (ii-vi) Successive fluorescence images of a rotating  $2.8\text{-}\mu\text{m}$  PS particle. Insets are schematic illustrations of the orientations of the rotor with two fluorescent nanoparticles as markers. Experimentally, two  $40\text{-nm}$  (in diameter) fluorescent PS nanoparticles were attached to the rotor through streptavidin-biotin bonding. The red point on the right side of the rotor marks the position of the driving laser beam. Scale bar:  $2\ \mu\text{m}$ . b, Time-dependent fluorescence intensity measured from the rotor and its surroundings as marked in a(iii). The out-of-plane rotation of the rotor leads to the periodic fluctuation of the fluorescence intensity. The intensity peaks appear when the rotation leads to both of fluorescent nanoparticles in the focal plane of the optical microscope.



**Figure 3**

Quantitative analysis and modelling of opto-thermoelectric rotation of single spherical rotors. a, Simulated magnitudes of depletion force and TE force along x axis on a 2.8- $\mu\text{m}$  PS particle as a function of PL distance in a 5% PEG/5% PBS solution. As marked by the dash line, a balance between depletion force and TE force (i.e., zero net force) is reached at a critical PL distance of 2.1  $\mu\text{m}$ . Inset: Schematic illustration of force analysis for the light-driven rotor in the xy plane. The red and white circles represent the laser spot and the rotor, respectively. b, Simulated torque (ME) acting on the rotor as a function of PL distance. The torque at the critical PL distance (2.1  $\mu\text{m}$ ) is around -1.6 pN $\cdot$ nm.

**Figure 4**

Parametric study and on-demand control of rotation behaviors. a, Rotation rate and critical PL distance of a 2.8- $\mu\text{m}$  PS particle versus PEG concentration in 5% PBS solutions at an optical power of 196  $\mu\text{W}$ . The grey squares and black line are experimentally measured (indicated as “EXP”) and simulated (indicated as “SIM”) rotation rates, respectively. The yellow diamonds and circles are measured and simulated

critical PL distances, respectively. b, Measured rotation rate of the PS particle in 5% PEG solutions with different PBS concentrations versus the optical power of laser beam. The dashed lines are linear fittings of the measured values. c, Measured and simulated torque and rotation rate as a function of particle size in a 5% PEG/5% PBS solution. The black dash line is linear fitting of the simulated torques. The red dashed line is the inverse cubic fitting of the simulated rotation rate. d, Simulated net forces along x axis of 1- $\mu\text{m}$  PS particles with different zeta potentials of -23, -38, and -47 mV in a 15% PEG/5% PBS solution, which lead to the different behaviors of the particles as illustrated in the insets

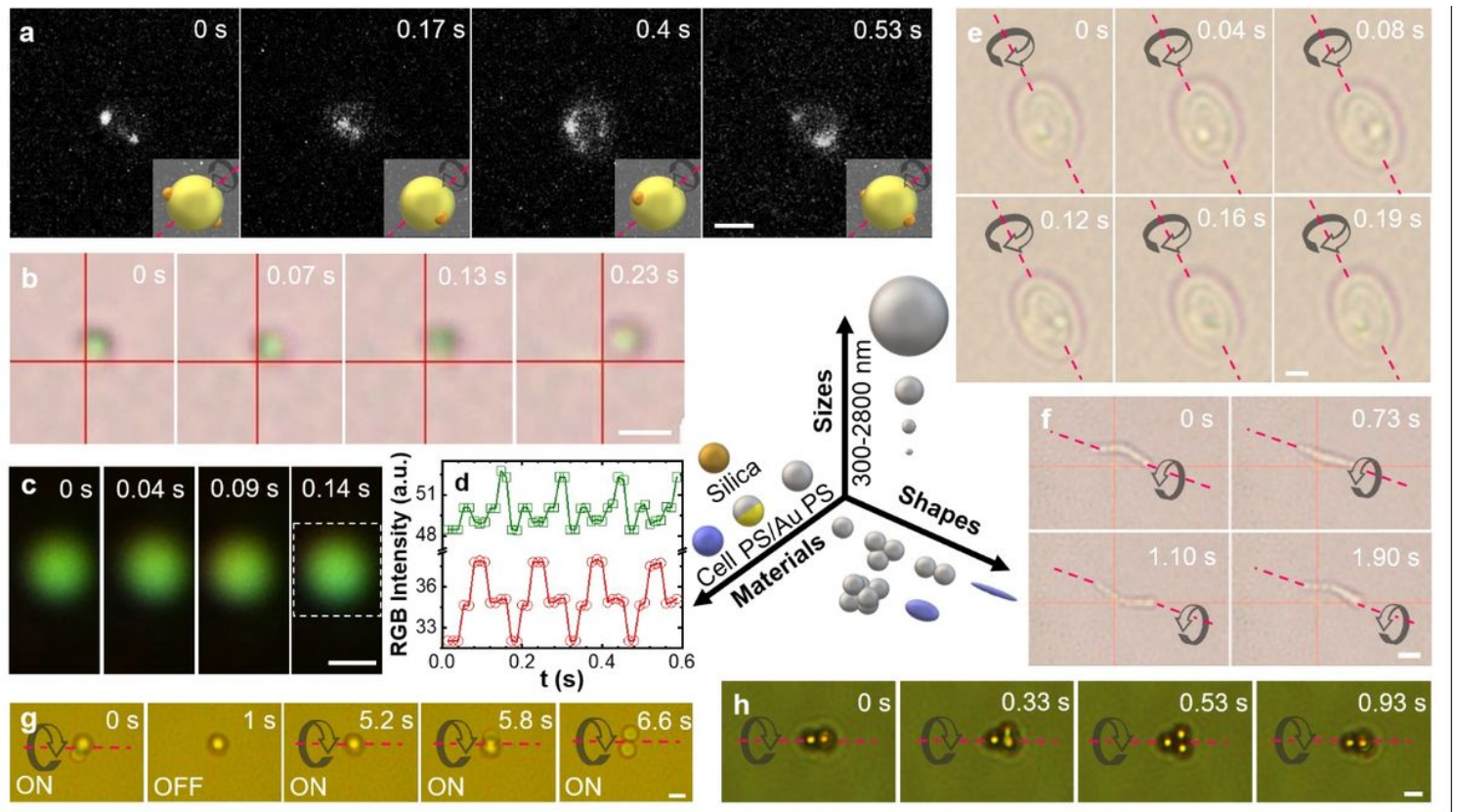


**Figure 5**

General applicability of opto-thermoelectric rotation to a variety of rotors with diverse shapes, sizes, and materials. a, Successive fluorescence images of a rotating 1- $\mu\text{m}$  PS particle labelled by fluorescent nanoparticles for the rotation visualization. b, Successive optical images of a rotating 500 nm PS/Au Janus particle. c, Successive dark-field optical images of a rotating 300 nm PS/Au Janus particle. d, Real-time RGB intensity of the dark-field optical images of the Janus particle. The white dash rectangle in c marks the selected area from which the RGB intensity is recorded. e, Successive optical images of a rotating yeast cell. f, Successive optical images of a rotating *B. subtilis*. g, Successive optical images of a rotating dimer composed of two 2- $\mu\text{m}$  silica particles. "ON" and "OFF" indicate that the laser beam is turned on and off, respectively. h, Successive optical images of a rotating trimer composed of three 1- $\mu\text{m}$  PS particles. The dash lines and black arrows represent the rotation axes and directions, respectively. Scale bars: a, b, e, f, h, 1  $\mu\text{m}$ ; c, 500 nm; g, 2  $\mu\text{m}$ . Solutions: a-c, g-h, 15% PEG/5% PBS; e-f, 5% PEG/5% PBS.

## Supplementary Files

This is a list of supplementary files associated with this preprint. Click to download.

- [RotorNat.PhotoSI1231.docx](#)
- [MovieS1.mov](#)
- [MovieS2.mov](#)
- [MovieS3.mov](#)
- [MovieS4.mov](#)
- [MovieS5.mov](#)
- [MovieS6.mov](#)
- [MovieS7.mov](#)
- [movieS8.mov](#)
- [MovieS9.mov](#)
- [MovieS10.mov](#)
- [MovieS11.mov](#)
- [MovieS12.mov](#)
- [MovieS13.mov](#)
- [MovieS14.mov](#)